

Reborn Three-Dimensional Graphene with Ultrahigh Volumetric Desalination Capacity

Yuanyuan Li, Nan Chen,* Zengling Li, Huibo Shao, Xiaotong Sun, Feng Liu,* Xiaoting Liu, Qiang Guo, and Liangti Qu*

The constructing of 3D materials with optimal performance is urgently needed to meet the growing demand of advanced materials in the high-tech sector. A distinctive 3D graphene (3DG) is designed based on a repeated rebirth strategy to obtain a better body and performance after each round of rebirth, as if it is Phoenix Nirvana. The properties of reborn graphene, namely 3DG after Nirvana (NvG), has been dramatically upgraded compared to 3DG, including high density (3.36 times) together with high porosity, as well as better electrical conductivity (1.41 times), mechanical strength (32.4 times), and ultrafast infiltration behavior. These advantages of NvG make it a strong intrinsic motivation for application in capacitive deionization (CDI). Using NvG directly as the CDI electrode, it has an extremely high volumetric capacity of 220 F cm^{-3} at 1 A cm^{-3} and a maximum salt adsorption capacity of $8.02\text{--}9.2 \text{ mg cm}^{-3}$ (8.9–10.2 times), while the power consumption for adsorption of the same mass of salt is less than a quarter of 3DG. The “Phoenix Nirvana”-like strategy of manufacturing 3D structures will undoubtedly become the new engine to kick-start the development of innovative carbon materials through an overall performance upgrade.

physicochemical properties designed to serve as functional materials, has always been respected by scientists. Compared to conventional distillation, reverse osmosis, and electro dialysis, capacitive deionization (CDI) operated with low energy input, low-pressure pumps, without membrane and no secondary waste is regarded as an auspicious ion removal technique for medium level investment and productivity,^[1–6] attracting enormous attention of researchers worldwide in the field of seawater and brackish water purification.^[7–10] The 3D microstructured electrode material, the core component of CDI, plays a decisive role in the performance and efficiency of deionization.

Generally, the gravimetric maximum salt adsorption capacity (g-mSAC) per unit mass of electrode materials is reported in CDI to understand the deionization performance of electrode materials.^[5,11]

1. Introduction

Wherever and whenever possible, how to fabricate 3D materials possessing a controlled artificial microstructure and optimum

In fact, the volumetric maximum salt adsorption capacity (v-mSAC) per unit volume of electrode material is often a more pertinent figure-of-merit to access real-world feasibility than blindly pursuing g-mSAC.^[12–14] Realizing high v-mSAC requires maximizing both the g-mSAC and physical density (ρ) of the electrode at the same time, which seems more difficult and extremely challenging because $v\text{-mSAC} = g\text{-mSAC} \times \rho$. However, there is typically a trade-off between g-mSAC and ρ that appears not to work both ways. For arbitrary conventional 3D materials, an increase in ρ is often inevitably accompanied by a decrease in porosity and specific surface areas (SSA), as well as a destruction of the 3D structure or even a weakening of the physicochemical properties, which are highly correlated with deionization performance. Porous materials with larger SSA contribute significantly to g-mSAC, but the reduction of ρ wastes pore space while reducing the mechanical strength and hydrophilicity of the material, all of which negatively affect the maximization of deionization capacitance. Therefore, synthesizing the CDI materials with high v-mSAC requires balancing several factors. In addition, conductive agents and binders that have a negative effect on porosity and CDI capacity^[15] are usually used to solve the problems of poor adhesion and low conductivity during electrode preparation.^[16–18] Designing new materials and constructing specific 3D microstructures of electrodes are of great significance for CDI technology.

Y. Li, N. Chen, Z. Li, H. Shao, X. Sun, X. Liu, Q. Guo

Key Laboratory of Cluster Science

Ministry of Education of China

Key Laboratory of Photoelectronic/Electrophotonic Conversion Materials

School of Chemistry and Chemical Engineering

Beijing Institute of Technology

Beijing 100081, P. R. China

E-mail: gabechain@bit.edu.cn

F. Liu

State Key Laboratory of Nonlinear Mechanics Institute of Mechanics

Chinese Academy of Sciences

Beijing 100190, P. R. China

E-mail: liufeng@imech.ac.cn

L. Qu

Key Laboratory of Organic Optoelectronics & Molecular Engineering


Ministry of Education

Department of Chemistry

Tsinghua University

Beijing 100084, China

E-mail: lqu@mail.tsinghua.edu.cn

 The ORCID identification number(s) for the author(s) of this article can be found under <https://doi.org/10.1002/adma.202105853>.

DOI: 10.1002/adma.202105853

For controllable artificial microstructured materials, 3D structured graphene is more flexible in tuning, based on which high SSA, extraordinary conductivity, and good mass transfer properties are formed,^[19,20] and is considered as a promising “metamaterial” and widely used, including in CDI.^[21–32] Self-assembled 3DG (3DG foam) obtained by such as hydrothermal, unfortunately, often face the pitfalls of large pore size and imprecise adjustment, resulting in wasted pore space.^[12] This has a negative effect on 3DG when it comes to utilizing the intrinsic talent of graphene. Uncontrollable or oversized pore sizes in 3DG limit the enhancement of g-mSAC and, worse, reduce v-mSAC, thus making CDI technology less valuable when oversized electrodes are used to meet the requirement of satisfactory desalination effect. The topology optimization design of 3D structured graphene is always challenging, although it is a proven way to fabricate “metamaterial” 3DG with high density and efficient ion storage properties.

Here, freeze-dried and crushed porous graphene particles (PGPs) and graphene chippings (GCs) are reassembled sequentially with graphene sheets to be reborn as structurally topologically optimized free-standing 3DG that can be called NvG. PGPs act as the “muscle” of NvG, which not only possesses a dense microstructure to ensure the high porosity of NvG, but also facilitates the effective ion adsorption and positively affects the mechanical properties of NvG based on the particle reinforced effect. The holey graphene sheets serve as a supporting “skeleton” of NvG, which achieves the uniform distribution of graphene “muscles” on the independent 3D skeleton structure and endows NvG with excellent mechanical properties. GCs obtained by grinding NvG^{*n*–1} (*n* represents the number of rebirth, *n* ≥ 2) acted as “ligament” bridging the graphene sheets, improving the microscopic morphology and mechanical properties of NvG^{*n*}. Consequently, the twice reborn NvGII delivers a high volumetric capacity of 220 F cm^{–3} at 1 A cm^{–3}, as well as a v-mSAC of 8.02 mg cm^{–3}, which is the highest value of all previously reported free-standing 3D carbon-based electrodes in CDI.

2. Results and Discussion

The reborn stage in the repeated rebirth strategy (RRS) for NvG preparation is shown in Figure 1a. As a precursor for preparing NvG, holey graphene hydrogel (HGH) monolith was optimally prepared by evaporation-induced dehydration of graphene hydrogel (Note S7 and Figures S1 and S2, Supporting Information, for detail). PGPs as pivotal material for reborn stage were subsequently produced by high-energy ball milling of HGH monolith. The PGPs in Figure 1e,f have an average diameter of about 1–3 μm with a denser structure and no visible openings. The PGPs observed from the TEM image show abundant in-plane pores with a diameter of about 5 nm, as shown by several yellow dashed circles in Figure 1g. The prolonged sonication treatment dispersed all the PGPs into graphene sheet structures and mixed them homogeneously with GO dispersions; the components are reborn into NvGI by targeted freeze-drying technique combined with low-temperature annealing treatment. The microscopic main structure of NvGI is similar to that of 3DG as shown in Figure 1b,c, and both consist of

vertically aligned graphene lamellar structure stacked on top of each other. However, the difference with 3DG is that the reborn strategy makes the interlayer spacing of NvGI smaller. Unlike the smooth graphene sheet surface of 3DG as shown in Figure 1d, PGPs are evenly dispersed on the surface of the vertically aligned graphene lamellar structure of NvGI, making its surface structure more complex, as shown in Figure S3, Supporting Information. For breaking through the limitation of graphene lamellar structure on the PGPs load-bearing capacity and further increasing the space utilization between vertically aligned graphene sheets, the above steps were repeated to crush the NvGI to obtain GCs consisting of graphene sheets loaded with PGPs as shown in Figure S4, Supporting Information. The GCs are immediately afterward added to the precursor solution for preparing NvGI to regenerate NvGII, which allows GCs from NvGI to be further filled between the vertically aligned graphene sheets of NvGII. After undergoing RRS, NvGII was sequentially attached to PGPs and GCs. Similarly, NvG^{*n*} (*n* ≥ 2) can be reborn from the GCs of NvG^{*n*–1} and possesses an enhancing effect on the performance of NvG^{*n*} at the same time.

NvGII offers many PGPs attached to graphene lamellar structure and displays no signs of distortion or destruction in the graphene skeleton structures. There are still abundant micron-sized pore channels on the surface as shown in Figure 1h,i, facilitating the rapid penetration and flow of liquids. In Figure 1j, we also find that the graphene sheet structure of NvGII in the yellow dashed circle is significantly thicker, which stems from the reinforcing effect of the PGPs and GCs introduced by the RRS to the 3D graphene structure. The freeze setting during RRS also causes the NvGII to present vertically aligned lamellar structures with spacing of tens of microns, as shown in Figure 1k,l, which is very helpful for the directional flow of the liquid. The magnified image of the NvGII vertical sheets shows more clearly that the artificially rendered purple PGPs in Figure 1m uniformly dispersed on the 3DG skeleton make the graphene sheet structure thicker, while the artificially rendered green GCs filled between the vertically aligned graphene lamellar structures in Figure 1n also serve as an effective tool for cross-linking and strengthening the 3DG skeleton. The TEM image of the small fragments of NvGII obtained by ultrasonic dispersion treatment is shown in Figure 1o. Both PGPs and GCs are firmly attached to the 2D monolayered graphene of NvGII (Figure 1p), fully confirming that the RRS allows strong bonding between the different functional graphene structures. The NvGII obtained by the RRS (twice in total) makes the skeletal-only 3DG stronger, as if it had gained muscle and ligament. This vivid comparison is as shown in Figure 1q for a very weak human skeleton alone and Figure 1r for a very strong human skeleton by muscles and ligaments attached.

Unlike typical 3DG made by hydrothermal method which undergoes shrinkage (Figure S5a,b, Supporting Information), it is possible to fabricate NvGs that fits exactly to the shape of the selected mold, such as circle, hexagonal star, ring and letters as shown in Figure 2a and Figure S5d, Supporting Information, enjoying sizable advantages indeed for the precision machining of 3D graphene. For batch production and practical applications, larger areas (≈230 cm² total area) of NvGII in Figure 2a have been developed using the RRS. The RRS has

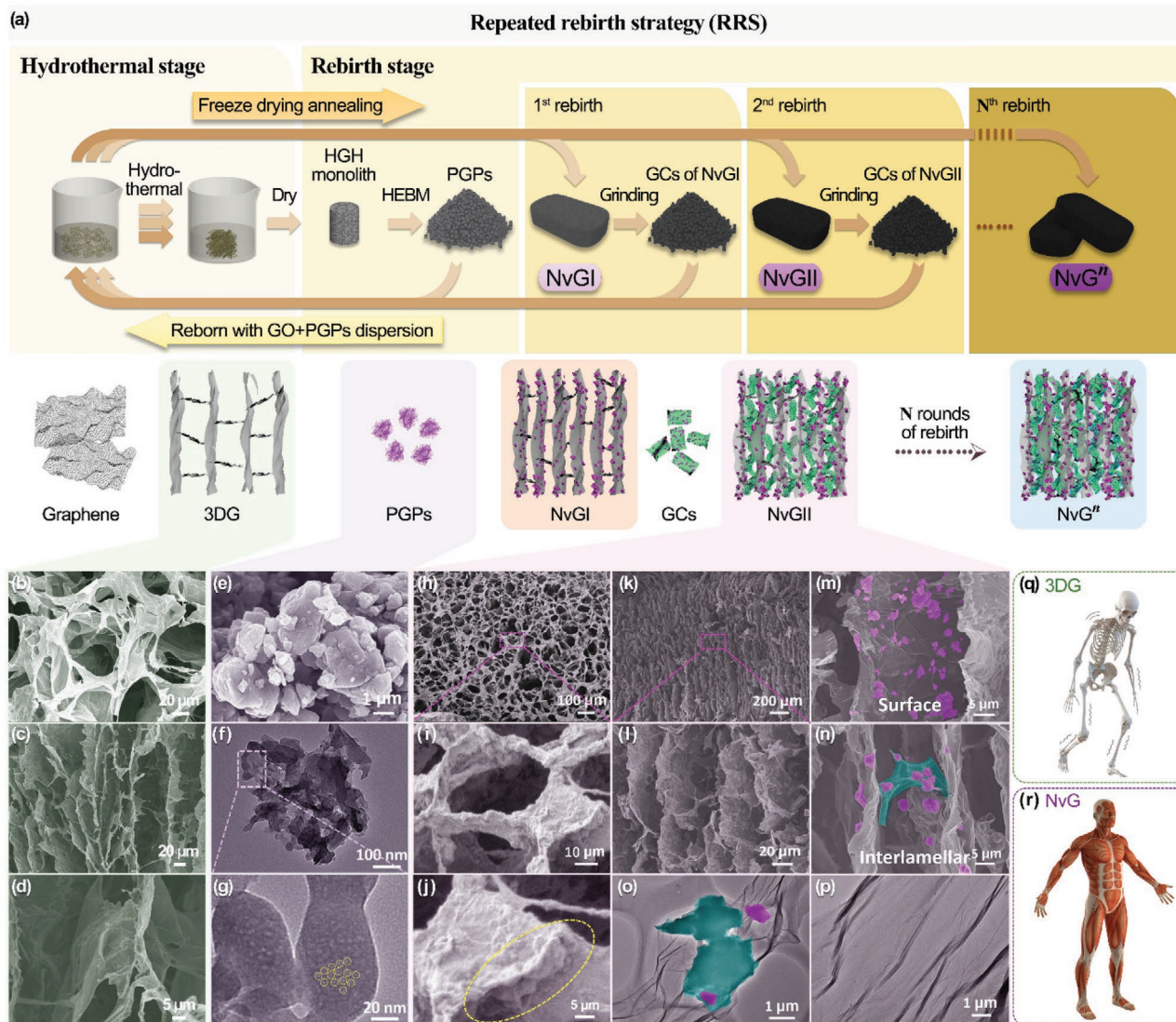


Figure 1. Preparation process of NvG^n and their microstructure. a) Flow chart of the RRS for preparing NvG^n , and schematic diagrams of the structure of the products obtained at each stage of the strategy. SEM images of the b) surface and c,d) cross section of a typical 3DG. e) SEM image and f) TEM image of PGPs. g) TEM image of PGPs at high magnification, where the holes on PGPs are shown in the yellow dashed circles. h,i) SEM image of $NvGII$. j) SEM image of the microstructure details of $NvGII$. k,l) SEM image of the cross section of $NvGII$. Microstructure of the m) surface and n) layer-to-layer of the graphene lamellar structure in $NvGII$. o,p) TEM images of $NvGII$. q) A typical 3DG as a human skeleton alone, while r) NvG^n ($n \geq 2$) is like a human skeleton by muscles and ligaments attached.

almost no effect on the porosity of $NvGII$, which still possess a high porosity (95.34%) compared to 3DG. The pore size distribution in Figure 2b shows that along with the reduction of pore area (Figure S6, Supporting Information), more micropores and mesopores appear in $NvGII$, which helps to avoid wasting pore space due to the presence of too many large pores. Raman spectroscopy in Figure 2c confirmed the chemical structure of graphene, where both 3DG and $NvGII$ are provided with typical D-band and G-band peaks at ≈ 1350 and ≈ 1590 cm^{-1} , respectively, representing large conjugated carbon system and structural defects in the graphite domains.^[33] The ratio of D-band to G-band intensity (I_D/I_G) in $NvGII$, which reflects the structure defects of graphene, is significantly smaller than that of typical 3DG, implying that more structural defects and active sites are

produced. X-ray diffraction in Figure 2d and Figure S7a, Supporting Information, shows that the typical sharp diffraction peak of GO in $NvGII$ at 11° disappears, producing a reduction peak at 24° .^[34] After RRS, the oxygen content in $NvGII$ decreases, a result that is likewise confirmed by X-ray photoelectron spectroscopy, as shown in Figure S7b, Supporting Information.

The correctness and uniqueness (Note S8 and Figure S8, Supporting Information) of the RRS is illustrated by comparing the conventional freeze-dried method of increasing the concentration of GO solution to prepare typical 3DG and the only once rebirth using increased PGPs incorporation of $NvGI$ as shown in Figure S9, Supporting Information. It is found that a higher density 3DG cannot be obtained by infinitely increasing

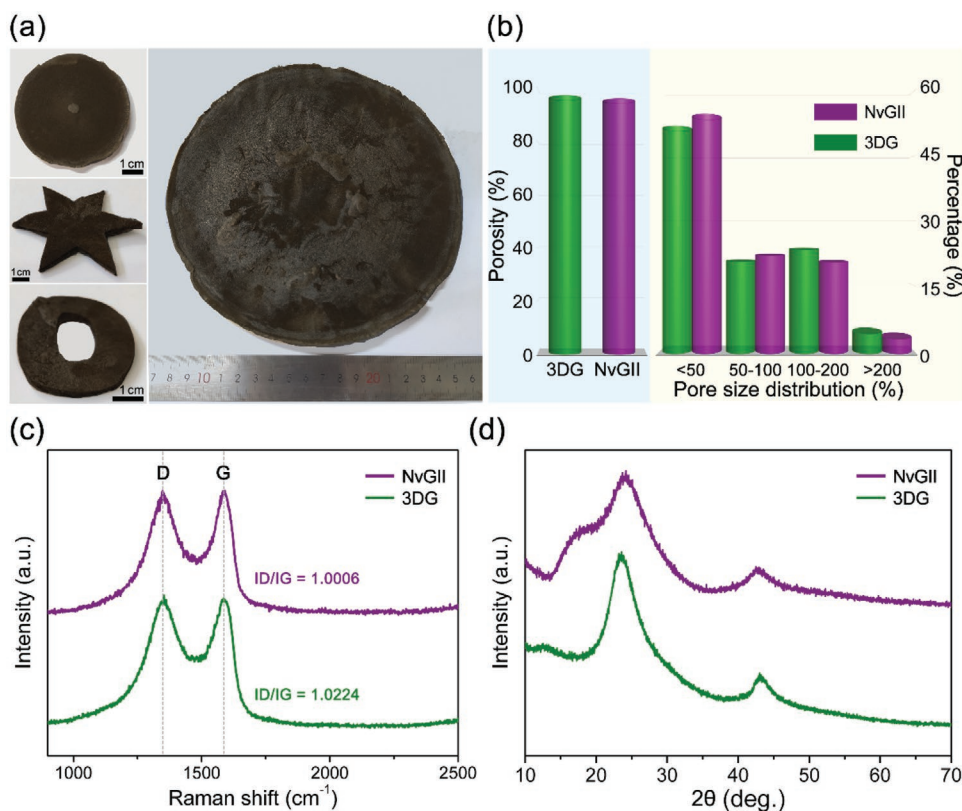


Figure 2. Characterization of NvGII. a) NvGII can be manufactured to the exact shape and size required. b) Porosity and pore size distribution of NvGII and 3DG. c) Raman spectra of NvGII and 3DG. d) XRD spectra of NvGII and 3DG.

the concentration of GO solution in the directly freeze-dried method, which has an upper density limit of 136.7 mg cm^{-3} as shown in Figure 3a, because it is difficult for a monolayer of GO to be concentrated by centrifugation to obtain a higher concentration of GO solution. For the only once rebirth, too many PGPs severely damage the original graphene 3D lamellae structure of NvGI, as shown in Figures S9a–d and S10a, Supporting Information, where they collapse and deform the graphene 3D lamellae structure. The density of NvGI prepared by adding the optimal amounts of PGPs was found to be 222.4 mg cm^{-3} , which is also the precursor to continue the production of NvGII by the second reborn strategy. Compared to typical 3DG and NvGI, the RRS allows NvGII with better microstructure (Figures S7e–h and S10b, Supporting Information) to obtain higher density ($459\text{--}678 \text{ mg cm}^{-3}$) while maintaining high porosity, as shown in Figure 3a. NvGII was chosen for further study because it is a typical NvGⁿ representative with enhanced properties while retaining the best microstructure due to the completion of two rebirths supplemented with PGPs and GCs in turn. It was found that NvGII has a qualitative leap in numerous physicochemical properties compared to typical 3DG, which must allow it to better exploit the advantages of graphene itself in practical applications. First, the electrical conductivity of the material is a key factor in the electrochemical process and can be measured by electrochemical impedance spectroscopy. In the Nyquist plots, as shown in Figure 3b, the charge transfer resistance (R_{ct}) of 3DG and NvGII are similar, whereas the R_s value of NvGII (2.25Ω) is significantly lower

than that of 3DG by about 30%, implying the NvGII displays faster ion diffusion speed.^[35,36]

The mechanical properties that contain stress–strain measures and simulation also revealed that the NvGII performs very well in terms of stability and reliability, which supports the ability of the NvGII to maintain an intact microarchitecture when subjected to external impacts, such as water flow. As shown in Figure 3c, the reinforcement effect of PGPs and the additional cross-linking stabilization of GCs would yield a larger area under the stress–strain curve, making a peak stress at much higher strain levels, specifically, NvGII can reach 68 kPa , much greater than the 2.1 kPa of the 3DG, showing higher toughness. Molecular dynamics simulations were performed to verify PGPs and GCs reinforcement mechanism. The theoretical simulation model is given in Figure 3d and Figure S11, Supporting Information, where graphene sheets are placed to form a square skeleton to which PGPs and GCs would be attached to or embedded in its surface. With careful reference to the multidirectional SEM images of NvGs and their test density, the parameters in the models used to perform the simulations were determined and four models were constructed (Note S9 and Figures S9, S12, and S13, Supporting Information). Figure 3e shows the potential stress distribution of the four models at 5% uniaxial tension. The reinforcement mechanism clearly shows that the graphene skeleton is tightly connected to the added PGPs compared to 3DG, which increases the mechanical strength of the NvGI as shown in Figure 3e(I,II). If the second reborn strategy is not

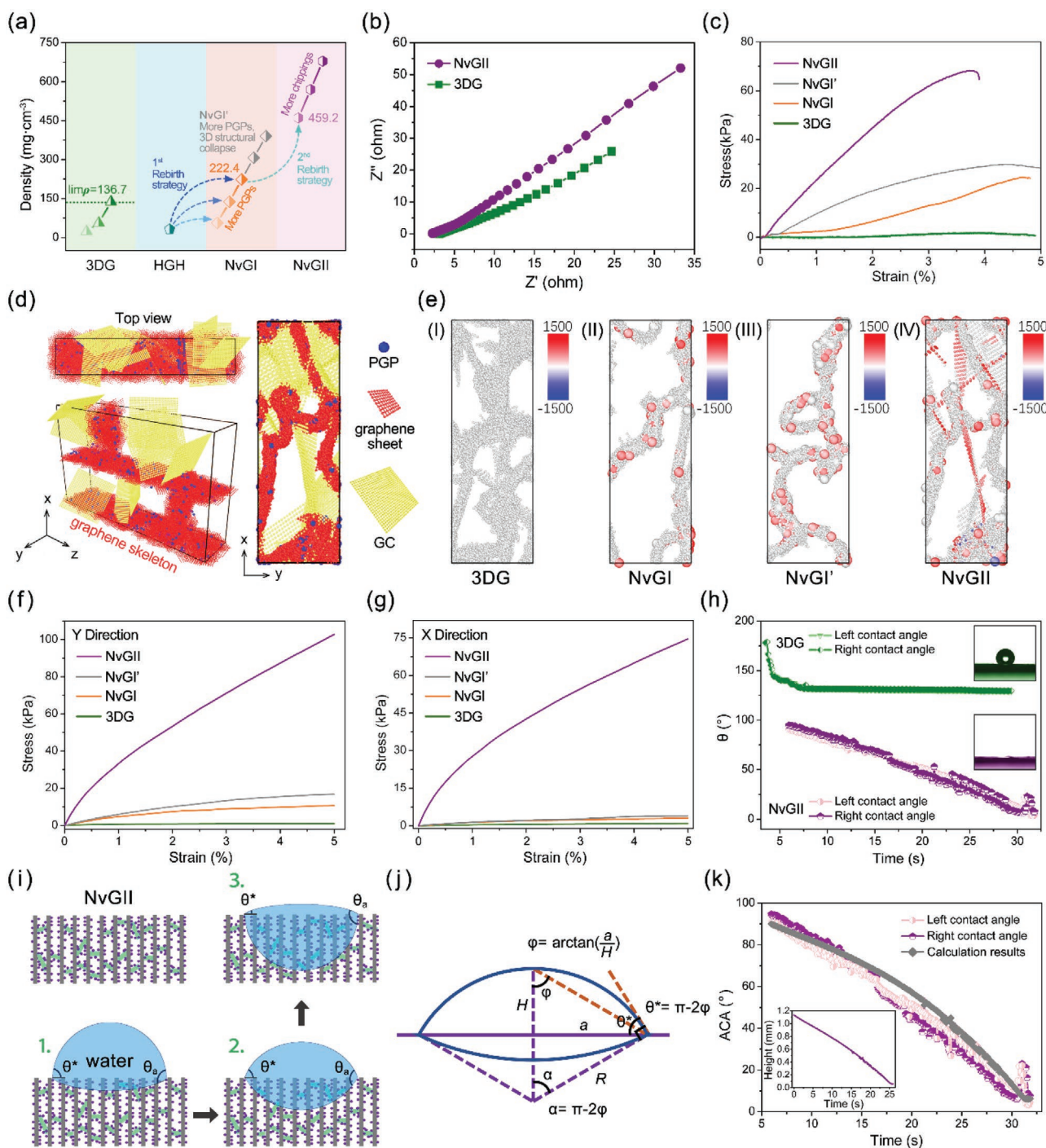


Figure 3. Physicochemical properties of NvG and its theoretical simulation. a) The densities of 3DG, NvGI, NvGI', and NvGII and the evolutionary relationship among them. b) Nyquist plots of 3DG and NvGII. c) The typical stress–strain curves of 3DG, NvGI, NvGI', and NvGII, respectively. d) The theoretical simulation of the NvGII 3D model in cubic space. On the right is a side view of NvGII in the z-axis direction. e) The potential energy distribution for 3DG, NvGI, NvGI', and NvGII, respectively. f, g) Corresponding strain and stress curves along the y-axis and x-axis directions, respectively. h) Measured apparent left and right contact angles of NvGII and 3DG. i) Schematic diagram of the water absorption process in NvGII, where the apparent contact angle (θ^*) and the actual contact angle (θ_a) are indicated separately, and θ_a is kept constant throughout the process. j) Geometric relationship between θ_a and height (H). k) The θ^* obtained from Equation (2) is compared with the experimentally measured θ^* . The inset shows the curve of the droplet height (H) as a function of time.

implemented and the NvGI' is prepared only by adding PGPs in excess at the first reborn strategy with reference to the

density of NvGII, the simulation results in Figure 3e(III) show that the increase of PGPs has very limited enhancement in the

mechanical strength of NvGI'. The toughness and stability of the NvGII structure, as shown in Figure 3e(IV), is enhanced by forming clusters of GCs within the graphene skeleton brought about by the second reborn strategy, and then forming additional cross-linking bonds between them. The stress and strain curves analyzed along the y -axis and x -axis directions are used to quantify the effect of PGP reinforcement and GCs cross-linking enhancement, as shown in Figure 3f,g. For a given effective strain along the y -axis, the stress of the NvGII model with PGPs and GCs was found to be about two orders of magnitude higher than those of the 3DG model, or 6 to 10 times larger than those of the NvGI and NvGI' models with different amounts of PGP only, which are in general agreement with the experimental result in Figure 3c. The simulation results well confirm the effectiveness of the RRS-induced particle enhancement and GCs cross-linking enhancement mechanisms. The stability and reutilization of electrode material under tough environmental conditions is an essential parameter for practical applications, and the additive manufacturing of attaching PGPs together with GCs as muscles and ligaments to the graphene skeleton will undoubtedly provide substantial technological advances.

The wetting behavior of water droplet on NvGII and 3DG surfaces was also investigated. In general, the wetting behavior of solids with the same chemical composition is governed by the surface geometrical microstructures. A typical 3DG is moderately hydrophobic with an apparent contact angle (θ^*) of 129° as shown in Figure 3h. Adding the fractal "muscle" and "ligament" allows the more complex NvGII structure no longer have θ^* ($=0^\circ$) within a short time after wetting with water droplet, meaning that a net positive effect occurs when the RRS is applied to the hydrophobic 3DG (Figure 3h and Movies S1 and S2, Supporting Information). The predefined internal microstructure of NvGII was further characterized by SEM to re-examine the great differences in the wetting behavior between NvGII and typical 3DG, as shown in Figure 1b.i. It is found that the graphene sheets in 3DG remain stretched flake sheets, while the corresponding ones in NvGII shrink into bundles owing to the large number of PGPs and GCs contacting the graphene sheets and wrap them. Although the surface macrotopology does not look much different, the substructure of NvGII becomes a more open-cell system than that of 3DG, inducing water to infiltrate into its interior more easily. The fraction of solid-liquid interface per unit area, f , and the roughness factor, R_f , are estimated based on SEM images, by using the contact angle equation proposed by Marmur.^[37]

$$\cos \theta^* = f(R_f \cos(\theta_0 + 1)) - 1 \quad (1)$$

where θ^* is known as the static water contact angle calculated from f and R_f . We obtained θ^* of 115° and 113° for 3DG and NvGII, respectively.^[38] The water absorption movement can facilitate the understanding of the change process of contact angle. Figure 3i illustrates the gradual capillary-driven entry of water into the topography-rich NvGII, with water in the center penetrating faster than water at the edge due to the height differences. It is assumed that the static wetting and water transport kinetics are decoupled throughout the infiltration process. Although the actual contact angle (θ_a) remains constant, the θ^*

measured experimentally decreases to zero with time, as shown by the markings in Figure 3i. The following geometrical relationship can be drawn based on the picture in Figure 3j,

$$\theta^* = \pi - 2 \cdot \arctan\left(\frac{a}{H}\right) \quad (2)$$

where a is the radius of the droplet and should be regarded as constant because it is observed experimentally to be almost constant during the infiltration process. H is the height of the droplet, whose evolution over time is shown in the inset of Figure 3k. Equation (2) is used to establish the apparent contact angle with respect to time and the result is shown in Figure 3k, which matches quite well with the experimental data. The simulation results quantitatively display the water absorption process, thus theoretically confirming the excellent wetting performance of NvGII, which is very helpful for the ion diffusion rate. 3DG was reborn to the higher self, giving NvG the numerous advantages of high electrical conductivity, strong mechanical properties, high porosity, good wettability, and short ion diffusion paths.

Major contribution to increased overall performance of NvGII comes from the developing of the RRS that yields NvGII with unparalleled advantages over graphene itself and/or typical 3DG, matching very well the characteristics of the electrode material required for CDI. The basic electrochemical behavior of the NvGII is measured before using it as an electrode for CDI (Note S10, Supporting Information). The electrochemical results show that the CV curves obtained for 3DG at a scanning rate of 10 mV s^{-1} as well as NvGI and NvGII electrodes with different densities have an almost symmetrical rectangular shape, as shown in Figure 4a, implying superior electric double layer (EDL) capacitance, and effective ion transport across the electrode surface. The optimized NvGII with a density of 459 mg cm^{-3} and a porosity of $382.5 \text{ m}^2 \text{ g}^{-1}$ was selected as a typical one for the electrochemical performance studies and subsequently served as CDI electrode because it offered the highest current density in the CV curve by achieving a well balance between the porosity and density.

The CV curves for NvGII in Figure 4b and Figure S14, Supporting Information, were measured at scan rates ranging from 1 to 200 mV s^{-1} over a potential range of 0–1 V. All the surface areas can be efficiently used for charge storage at low scan rates, which makes CV curves maintain typical rectangular. The shape of the CV curves becomes progressively leaf-like shape at higher scan rates due to the ions diffusion and accumulation in the electrode becoming somewhat difficult in the electrode along with the blocked ion transport formed by not very efficient formation of EDLs. Although the CV curves are not rectangular at high scan rates, they are also typical EDL capacitance and show reversible capacitive properties. The absence of a peak on CV curve in NvGII indicates neither oxidation nor reduction processes but the charge accumulation in the EDL as well. Specific capacitance measurements of NvGII were used to evaluate the electrochemical performance under different current densities, as shown in Figure 4c,d. The high porosity bonded with the high density brought about by the RRS allows NvGII to deliver a specific gravimetric capacitance of 198 F g^{-1} , which is at the forefront of many optimized 3D

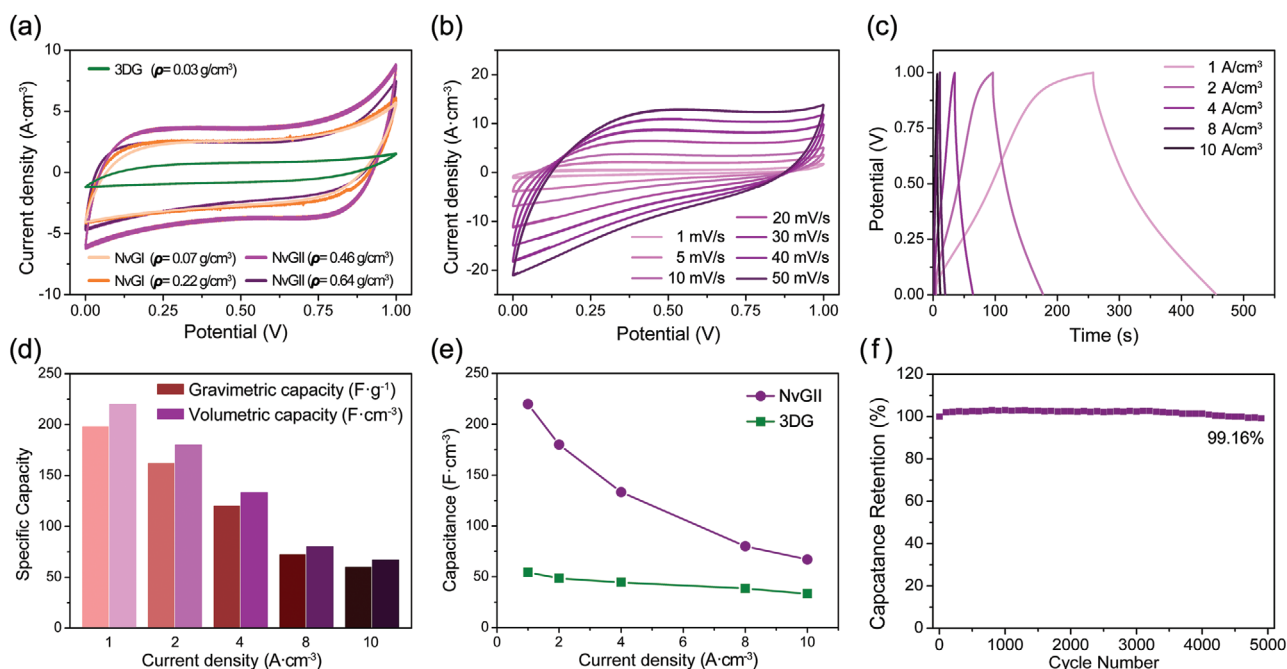


Figure 4. Electrochemical properties of NvGII. a) CV curves collected for 3DG as well as NvGI and NvGII with different densities at scan rate of 10 mV s⁻¹. b) CV curves of NvGII at different scan rates. c) GCD curves of NvGII at different current densities. d) Gravimetric and volumetric capacitances of NvGII at different current densities. e) Specific capacitances of NvGII at current densities ranging from 1 to 10 A cm⁻². f) Cycling stability of NvGII for 5000 cycles at a scan rate of 100 mV s⁻¹.

carbon materials, and a specific volumetric capacitance of up to 220 F cm⁻³ at 1 A cm⁻² (Figure 4e and Figures S15 and S16, Supporting Information) that is substantially ahead of previously reported typical free-standing 3D carbon-based CDI electrodes.^[39–50] Cycling stability test evaluates the electrode lifetime of the CDI electrode. The long-term cycling stability of the NvGII electrode was measured by CV curves at a scan rate of 100 mV s⁻¹, as shown in Figure 4f, where 99.3% of its initial capacitance was retained after 5000 cycles, except for a slight increase in capacitance observed during the initial cycling due to electrode activation.

Pressing free-standing NvGII into the CDI set-up (Figure S17, Supporting Information), the good flexibility brought by the “muscle” and “ligament” enhancement allows NvGII to sustain its 3D graphene skeleton without collapsing, where the microstructure in NvGII becomes squeezed and bent but remains strong (Figures S18 and S19, Supporting Information). After applying voltage, counter ions enter the micropores of the electrodes and are stored in the EDLs. When the voltage is switched off or the reverse voltage is applied, the electrically adsorbed ions are desorbed into the feed water as shown in Figure 5a, and the reuse of the NvGII electrode is achieved by repeating the above process. Applying an operating voltage of 2.0 V (Note S12 and Figure S20, Supporting Information),^[51] the v-mSAC of NvGII with the best electrochemical performance was also the highest, with a value of 8.02 mg cm⁻³ in a 500 mg/L NaCl solution as shown in Figure 5b and Figure S21, Supporting Information. The huge advantage of v-mSAC in CDI obtained through the development of the RRS prompted us to study the characteristics of successive generations of NvG, including NvGI, NvGII, and even NvGIII. Adjusting the devty

of each generation of NvG and accounting for clustering by their seniority in the NvG family show that first the increase of density accompanied by the increase of PGPs addition makes the v-mSAC performance of NvGI electrode gradually increase to the maximum. By continuing to add PGPs, the vertically oriented structure of the obtained higher density NvGI' collapses and hinders the effective diffusion and transport of ions in it, resulting in lower v-mSAC performance than NvGI. NvGII and NvGIII, obtained sequentially from the reborn strategy of NvGI and NvGII, have higher v-mSAC of 8.02 and 9.2 mg cm⁻³, respectively, which are 8.9 and 10.2 times higher than those of typical 3DG (0.9009 mg cm⁻³). The RRS gave the progenys of NvGI, namely NvGII and NvGIII, a superior structure and higher volumetric desalination capacity, which is an overlay effect of the structural enhancement of PGPs and the cross-linking stabilization of GCs.

The RRS resulted in successive generations of NvG (NvGⁿ, $n \geq 2$) exhibiting similar properties, and therefore NvGII was selected as the typical one for follow-up CDI studies from the consideration of efficiency of preparation. CDI performance in terms of reversibility of electrosorption-desorption cycles of ions by NvGII was carried out in 500 mg L⁻¹ NaCl solution with several sets of typical voltage values selected between 1.0 and 2.0 V to observe the stability of the electrosorption-desorption process of NvGII as shown in Figure 5c and Figure S22a, Supporting Information. Each of the electrosorption-desorption test was performed at different voltage values until little change in conductivity was observed. A positive correlation was found between voltage and electrosorption capacity of salt ions^[18] mainly due to stronger Coulomb interactions and the enhanced EDLC performance. The application of a reverse voltage during

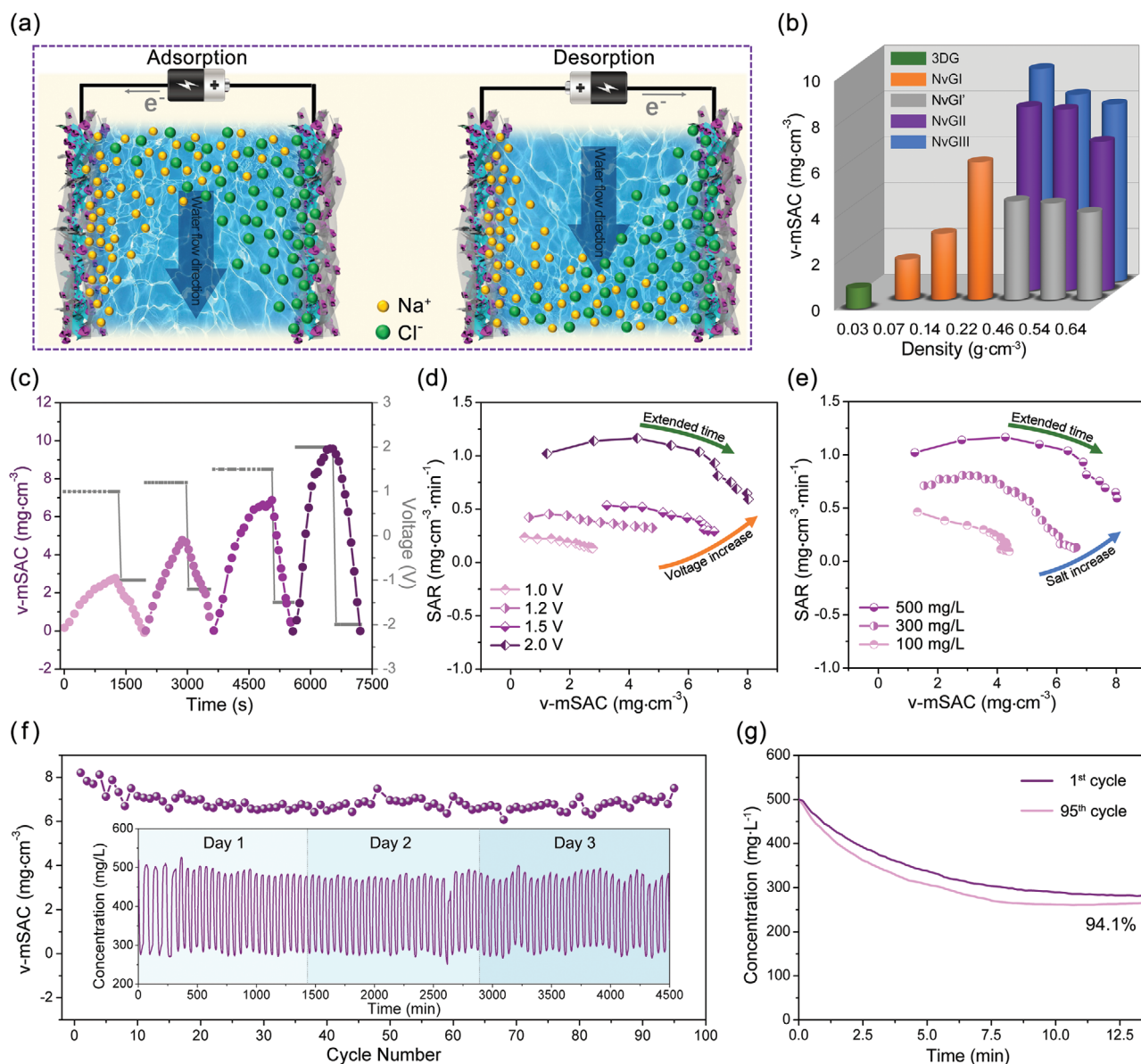


Figure 5. CDI performance of NvG. a) Schematic diagram of CDI process. b) The comparison v-mSAC of 3DG, NvGI, NvGI', NvGII, and NvGIII with different densities. c) Electrosorption–desorption cycles of NvGII in 500 mg L⁻¹ NaCl solution at sequentially of 1.0, 1.2, 1.5, and 2.0 V. d,e) Ragone plots of NvGII in the above applied voltage (d) and in different concentrations of NaCl solutions (e). f) Electroadsorption and long-term regeneration cycles of NvGII in 500 mg L⁻¹ NaCl solution at 2.0 V. g) Comparison of NaCl solution concentration as a function of time during the 1st cycle and the 95th cycle of the desalination process.

each electrosorption–desorption process can release salt ions into the solution in time and completely, providing further evidence of the good reversibility of the NvGII electrode. The CDI Ragone plots obtained by plotting salt adsorption rate (SAR) against v-SAC depicted in Figure 5d exhibit that the desalination rate is higher at higher operating voltages.

The same phenomenon was observed on varying the concentration of NaCl solution. Because at higher salinities, the transport flux of ions inside the NvGII increases is accompanied by a decrease in resistance (with a higher initial current, Figure S22b, Supporting Information), making the electrosorption capacity larger. The Ragone plots of CDI in Figure 5e exhibit that treating higher concentrations of NaCl shifts the

Ragone curve toward the upper right region, indicating that allowing NvGII to treat higher concentrations of NaCl causes it to exhibit higher desalination capacity and desalination rate. When the NaCl solution concentration was increased from 100 to 500 mg L⁻¹, the electroabsorption capacity increased from 4.2 to 8.02 mg cm⁻³, as shown in Figure S22c, Supporting Information. However, the v-SAC of NvGII was not further increased by the co-ion expulsion effect with increasing concentration of NaCl solution,^[52,1] as shown in Figure S23, Supporting Information. In addition, the effect of flow rate on the deionization performance was also investigated and the optimal flow rate for CDI testing was determined to be 15 mL min⁻¹ (Figure S24, Supporting Information).

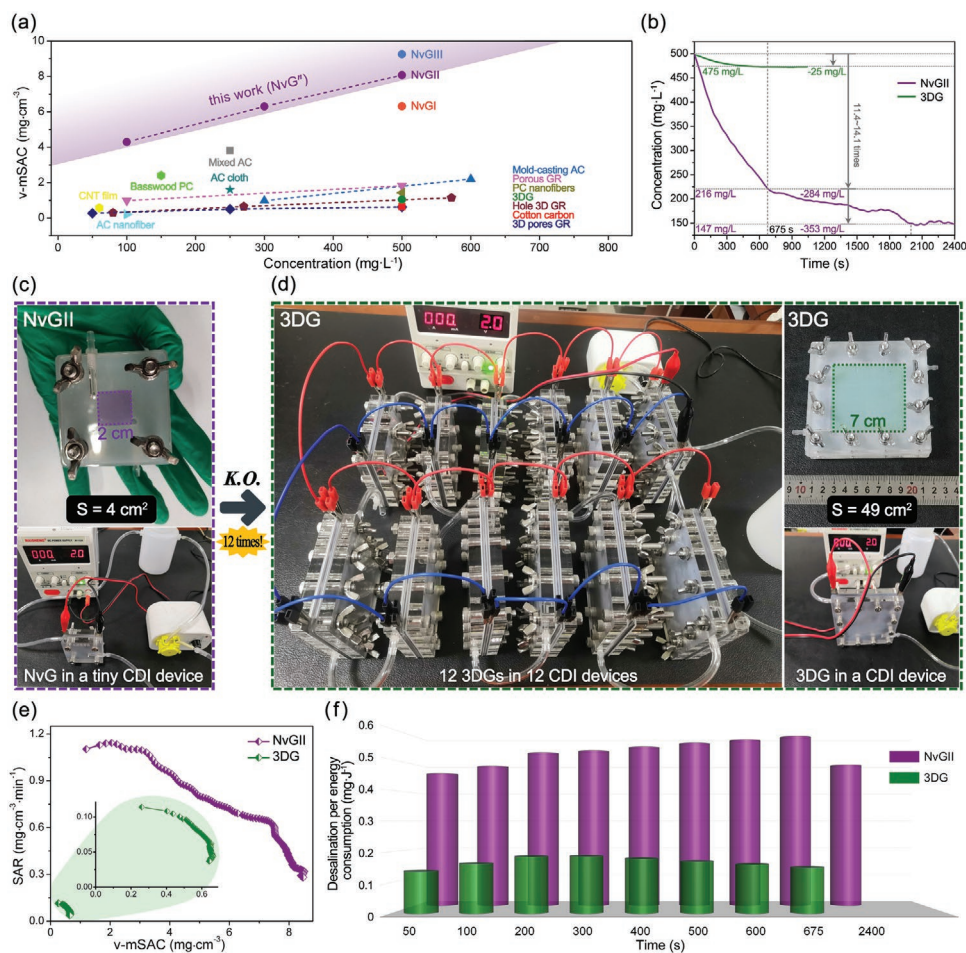


Figure 6. The awesome practical applications of NvGII. a) Comparison of NvGⁿ with previously reported free-standing 3D carbon-based CDI electrodes for v-mSAC. b) Comparison of the desalination effect of 3DG and NvGII in 500 mg L⁻¹ NaCl solution at 2.0 V. c,d) A tiny CDI device was designed using a small size of NvGII (4 cm²) with the same electrode thickness, which has 12 times the desalination capacity of a 3DG-based CDI device of the same size, or one-twelfth the size of one conventional 3DG electrode (49 cm²). e) Ragone plots of NvGII, 3DG, and other free-standing 3D carbon-based materials. f) The desalination per energy consumption of 3DG and NvGII.

The NvGII electrode exhibited high cycling stability and could be used repeatedly for 95 cycles as shown in Figure 5f and Figure S22d, Supporting Information, with only a 6% decrease in capacity after 3 days of electrosorption–desorption, and was able to reach the maximum electrosorption capacity in less than 13 min (Figure 5g), showing rapid kinetics and stable salt adsorption. NvGII retains its free-standing structure after cycling, with an intact appearance and no collapse of the microstructure and still has an oriented structure (see Figure S25, Supporting Information), indicating excellent structure stability. Carbon leaching experiments were performed to verify its stability in use. NvGII electrode was scoured at 15 mL min⁻¹ for 5 days without loss of mass and the structure remained intact, and the same results were obtained for other flow rates, as shown in Figure S26, Supporting Information.

The excellent CDI performance of NvGII is visualized in Figure 6a, where the v-mSAC of NvGII is already the highest value previously reported for binder-free carbon-based 3D electrodes (Note S12 and Figures S27 and S28, Supporting Information).^[16,53–66] Not to be overlooked, the v-mSAC of NvGIII is even higher, with a value of 9.2 mg cm⁻³, which is

10.2 times of that of a typical 3DG. Desalination tests were performed in a 500 mg L⁻¹ salt solution using the same size of 3DG and NvGII as CDI electrodes as shown in Figure 6b. The desalination capacity of NvGII was much higher than that of typical 3DG, allowing a reduction of the salt solution concentration by 284 mg L⁻¹ in 675 s (11.4 times that of 3DG), while in contrast, the desalination capacity of 3DG saturated at 675 s without allowing the salt solution concentration to drop further (eventually by a total of 25 mg L⁻¹). Continuing with the desalination, the NvGII was able to reduce the salt solution concentration to 147 mg L⁻¹, which was 14.1 times higher than that of the 3DG. It is as if in a CDI device using only 1 NvGII electrode has completely beat the desalination capacity of a dozen CDI devices assembled from the same size 3DG electrodes in parallel (e.g., it takes 12 3DG electrodes in parallel to catch up with the desalination capacity of 1 NvGII electrode in Figure 6d). As shown in Figure 6c, the small and powerful NvGII as a tiny CDI device is well suited to meet the needs of device integration and miniaturization today. The Ragone plots in Figure 6e and Figure S29, Supporting Information, more visually compare the desalination capacity of NvGII with typical 3DG, previously

reported free-standing 3D carbon-based electrodes, showing that the NvGII electrode possesses extremely high v-SAC and very fast v-SAR. In addition, energy consumption is also an important measure in the performance of CDI (Figure S30, Supporting Information). As in Figure 6f, we calculated the average of desalination per energy consumption (\bar{Q}) for NvGII and typical 3DG in 675 s, respectively. From start to finish, the \bar{Q} of NvGII is higher than that of 3DG, reaching 4.1 times that of 3DG within 675 s: $\bar{Q}_{\text{NvGII}} = 0.61 \text{ mg J}^{-1} > \bar{Q}_{\text{3DG}} = 0.15 \text{ mg J}^{-1}$. NvGII's low energy consumption is very much in line with the concept of global energy saving and green systems.

3. Conclusions

By constructing PGPs “muscle” and GCs “ligament” sequentially on graphene “skeleton” using the RRS, a reborn 3DG (NvG) with significantly improved overall performance was fabricated. NvG displays high density together with high porosity, as well as better electrical conductivity, mechanical strength, and wettability, making NvG sure enough to play irreplaceable advantages contrasted with that of typical 3DG in many areas. These advantages immediately make NvG stand out among CDI electrodes with a volumetric capacity of up to 220 F cm^{-3} at 1 A cm^{-3} and v-mSAC of $8.02\text{--}9.2 \text{ mg cm}^{-3}$ (8.9–10.2 times of typical 3DG), which is undoubtedly very superior to other free-standing 3D carbon-based CDI electrodes reported previously. The creativeness of fabrication strategy and the particularity of microstructure invariably confirm the advanced nature of the “Phoenix Nirvana” graphene. RRS used to fabricate distinctive 3D structures not only tailors to a powerful technical tool for the future CDI research, but more importantly, significantly changes the research methods and mindset of fabricating high-performance individually composed 3DG and even other typical 3D materials.

Supporting Information

Supporting Information is available from the Wiley Online Library or from the author.

Acknowledgements

This work was supported by the National Key R&D Program of China (2017YFB1104300 and 2016YFA0200200), NSFC (No. 21671020, 51673026, 22035005, 52073159, 11972349, and 11790292), NSFC-MAECI (51861135202), and Analysis & Testing Center of Beijing Institute of Technology, Strategic Priority Research Program of the Chinese Academy of Sciences (XDB22040503).

Conflict of Interest

The authors declare no conflict of interest.

Data Availability Statement

Research data are not shared.

Keywords

capacitive deionization, phoenix nirvana, reborn, three-dimensional graphene

Received: July 28, 2021

Revised: August 26, 2021

Published online: September 24, 2021

- [1] M. E. Suss, V. Presser, *Joule* **2018**, 2, 10.
- [2] W. Shi, X. Liu, T. Deng, S. Huang, M. Ding, X. Miao, C. Zhu, Y. Zhu, W. Liu, F. Wu, C. Gao, S. W. Yang, H. Y. Yang, J. Shen, X. Cao, *Adv. Mater.* **2020**, 32, 1907404.
- [3] H. Yin, S. Zhao, J. Wan, H. Tang, L. Chang, L. He, H. Zhao, Y. Gao, Z. Tang, *Adv. Mater.* **2013**, 25, 6270.
- [4] J. Li, B. Ji, R. Jiang, P. Zhang, N. Chen, G. Zhang, L. Qu, *Carbon* **2018**, 129, 95.
- [5] S. K. Patel, C. L. Ritt, A. Deshmukh, Z. Wang, M. Qin, R. Epszstein, M. Elimelech, *Energy Environ. Sci.* **2020**, 13, 1694.
- [6] X. Gao, S. Porada, A. Omosebi, K.-L. Liu, P. Biesheuvel, J. Landon, *Water Res.* **2016**, 92, 275.
- [7] M. Metzger, M. M. Besli, S. Kuppan, S. Hellstrom, J. Christensen, *Energy Environ. Sci.* **2020**, 13, 1544.
- [8] Y. Liu, X. Gao, K. Wang, X. Dou, L. Pan, *J. Mater. Chem. A* **2020**, 8, 8476.
- [9] J. G. Gamaethiralalage, K. Singh, S. Sahin, J. Yoon, L. Smet, *Energy Environ. Sci.* **2021**, 14, 1095.
- [10] B. Wta, L. Jie, H. Di, B. Jga, T. Lin, B. Zla, B. Dwa, B. Gza, *Water Res.* **2019**, 150, 225.
- [11] Q. Wang, J. Yan, Z. Fan, *Energy Environ. Sci.* **2016**, 9, 729.
- [12] Z. Li, S. Gadipelli, H. Li, C. A. Howard, D. J. Brett, P. R. Shearing, Z. Guo, I. P. Parkin, F. Li, *Nat. Energy* **2020**, 5, 160.
- [13] Y. Bu, T. Sun, Y. Cai, L. Du, O. Zhuo, L. Yang, Q. Wu, X. Wang, Z. Hu, *Adv. Mater.* **2017**, 29, 1700470.
- [14] M. Suss, S. Porada, X. Sun, P. Biesheuvel, J. Yoon, V. Presser, *Energy Environ. Sci.* **2015**, 8, 2296.
- [15] M. Ding, K. K. Bannuru, Y. Wang, L. Guo, A. Baji, H. Y. Yang, *Adv. Mater. Technol.* **2018**, 3, 1800135.
- [16] S. Vafakhah, L. Guo, D. Sriramulu, S. Huang, M. Saeedikhani, H. Y. Yang, *ACS Appl. Mater. Interfaces* **2019**, 11, 5989.
- [17] J. S. Kang, S. Kim, D. Y. Chung, Y. J. Son, K. Jo, X. Su, M. J. Lee, H. Joo, T. A. Hatton, J. Yoon, Y. E. Sung, *Adv. Funct. Mater.* **2019**, 30, 1909387.
- [18] C.-L. Yeh, H.-C. Hsi, K.-C. Li, C.-H. Hou, *Desalination* **2015**, 367, 60.
- [19] H. Huang, H. Shi, P. Das, J. Qin, Y. Li, X. Wang, F. Su, P. Wen, S. Li, P. Lu, *Adv. Funct. Mater.* **2020**, 30, 1909035.
- [20] Y. Sun, Z. Chen, H. Gong, X. Li, Z. Gao, S. Xu, X. Han, B. Han, X. Meng, J. Zhang, *Adv. Mater.* **2020**, 32, 2002024.
- [21] M. Peng, Z. Wen, L. Xie, J. Cheng, Z. Jia, D. Shi, H. Zeng, B. Zhao, Z. Liang, T. Li, *Adv. Mater.* **2019**, 31, 1902930.
- [22] H. J. Qiu, P. Du, K. Hu, J. Gao, H. Li, P. Liu, T. Ina, K. Ohara, Y. Ito, M. Chen, *Adv. Mater.* **2019**, 31, 1900843.
- [23] H. Li, T. Lu, L. Pan, Y. Zhang, Z. Sun, *J. Mater. Chem.* **2009**, 19, 6773.
- [24] H. Li, L. Zou, L. Pan, Z. Sun, *Environ. Sci. Technol.* **2010**, 44, 8692.
- [25] X. Xu, L. Pan, Y. Liu, T. Lu, Z. Sun, *J. Colloid Interface Sci.* **2015**, 445, 143.
- [26] X. Xu, Z. Sun, D. H. Chua, L. Pan, *Sci. Rep.* **2015**, 5, 11225.
- [27] X. Xu, Y. Liu, M. Wang, X. Yang, C. Zhu, T. Lu, R. Zhao, L. Pan, *Electrochim. Acta* **2016**, 188, 406.
- [28] L. Chang, Y. Fei, Y. H. Hu, *J. Mater. Chem. A* **2021**, 9, 1429.
- [29] M. A. Radi, E. T. Sayed, H. Alawadhi, M. A. Abdelkareem, *Crit. Rev. Environ. Sci. Technol.* **2021**, 130001.

- [30] J. Kang, J. Min, S. I. Kim, S. W. Kim, J. H. Jang, *Mater. Today Energy* **2020**, *18*, 100502.
- [31] Y. Zhu, G. Zhang, C. Xu, L. Wang, *ACS Appl. Mater. Interfaces* **2020**, *12*, 29706.
- [32] Y. Zhang, L. Chen, S. Mao, Z. Sun, Y. Song, *J. Colloid Interface Sci.* **2018**, *536*, 252.
- [33] S. Pei, Q. Wei, K. Huang, H.-M. Cheng, W. Ren, *Nat. Commun.* **2018**, *9*, 145.
- [34] J. Zhao, Y. Z. Zhang, F. Zhang, H. Liang, F. Ming, H. N. Alshareef, Z. Gao, *Adv. Energy Mater.* **2019**, *9*, 1803215.
- [35] W. Dianbudiyanto, S.-H. Liu, *Desalination* **2019**, *468*, 114069.
- [36] Z. He, F. Mansfeld, *Energy Environ. Sci.* **2009**, *2*, 215.
- [37] A. Marmur, *Langmuir* **2003**, *19*, 8343.
- [38] E. Singh, Z. Chen, F. Houshmand, W. Ren, Y. Peles, H. M. Cheng, N. Koratkar, *Small* **2013**, *9*, 75.
- [39] L. Zhang, F. Zhang, X. Yang, G. Long, Y. Wu, T. Zhang, K. Leng, Y. Huang, Y. Ma, A. Yu, *Sci. Rep.* **2013**, *3*, 1408.
- [40] M. F. El-Kady, V. Strong, S. Dubin, R. B. Kaner, *Science* **2012**, *335*, 1326.
- [41] Y. Xu, Z. Lin, X. Huang, Y. Liu, Y. Huang, X. Duan, *ACS Nano* **2013**, *7*, 4042.
- [42] C. Liu, Z. Yu, D. Neff, A. Zhamu, B. Z. Jang, *Nano Lett.* **2010**, *10*, 4863.
- [43] A. Izadi-Najafabadi, S. Yasuda, K. Kobashi, T. Yamada, D. N. Futaba, H. Hatori, M. Yumura, S. Iijima, K. Hata, *Adv. Mater.* **2010**, *22*, E235.
- [44] M. D. Stoller, S. Park, Y. Zhu, J. An, R. S. Ruoff, *Nano Lett.* **2008**, *8*, 3498.
- [45] X. Wang, C. Lu, H. Peng, X. Zhang, Z. Wang, G. Wang, *J. Power Sources* **2016**, *324*, 188.
- [46] Z. S. Wu, A. Winter, L. Chen, Y. Sun, A. Turchanin, X. Feng, K. Müllen, *Adv. Mater.* **2012**, *24*, 5130.
- [47] L.-F. Chen, Z.-H. Huang, H.-W. Liang, W.-T. Yao, Z.-Y. Yu, S.-H. Yu, *Energy Environ. Sci.* **2013**, *6*, 3331.
- [48] X. Chen, L. Qiu, J. Ren, G. Guan, H. Lin, Z. Zhang, P. Chen, Y. Wang, H. Peng, *Adv. Mater.* **2013**, *25*, 6436.
- [49] C. Choi, J. A. Lee, A. Y. Choi, Y. T. Kim, X. Lepró, M. D. Lima, R. H. Baughman, S. J. Kim, *Adv. Mater.* **2014**, *26*, 2059.
- [50] Y. Meng, Y. Zhao, C. Hu, H. Cheng, Y. Hu, Z. Zhang, G. Shi, L. Qu, *Adv. Mater.* **2013**, *25*, 2326.
- [51] Z. Li, B. Song, Z. Wu, Z. Lin, Y. Yao, K.-S. Moon, C. Wong, *Nano Energy* **2015**, *11*, 711.
- [52] M. Suss, S. Porada, X. Sun, P. Biesheuvel, J. Yoon, V. Presser, *Energy Environ. Sci.* **2015**, *8*, 2296.
- [53] G. Wang, C. Pan, L. Wang, Q. Dong, C. Yu, Z. Zhao, J. Qiu, *Electrochim. Acta* **2012**, *69*, 65.
- [54] W. Shi, H. Li, X. Cao, Z. Y. Leong, J. Zhang, T. Chen, H. Zhang, H. Y. Yang, *Sci. Rep.* **2016**, *6*, 18966.
- [55] H. Duan, T. Yan, G. Chen, J. Zhang, L. Shi, D. Zhang, *Chem. Commun.* **2017**, *53*, 7465.
- [56] Y. Xue, J. Xie, M. He, M. Liu, M. Xu, W. Ni, Y.-M. Yan, *J. Mater. Chem. A* **2018**, *6*, 19210.
- [57] M. Liu, M. Xu, Y. Xue, W. Ni, S. Huo, L. Wu, Z. Yang, Y.-M. Yan, *ACS Appl. Mater. Interfaces* **2018**, *10*, 31260.
- [58] H. Pan, J. Yang, S. Wang, Z. Xiong, W. Cai, J. Liu, *J. Mater. Chem. A* **2015**, *3*, 13827.
- [59] G. Wang, B. Qian, Y. Wang, Q. Dong, F. Zhan, J. Qiu, *New J. Chem.* **2016**, *40*, 3786.
- [60] X. Gao, J. Landon, J. K. Neathery, K. Liu, *J. Electrochem. Soc.* **2013**, *160*, E106.
- [61] M. T. Z. Myint, S. H. Al-Harhi, J. Dutta, *Desalination* **2014**, *344*, 236.
- [62] L. Wu, M. Liu, S. Huo, X. Zang, M. Xu, W. Ni, Z. Yang, Y. M. Yan, *Carbon* **2019**, *149*, 627.
- [63] F. Ji, L. Wang, J. Yang, X. Wu, M. Li, S. Jiang, S. Lin, Z. Chen, *J. Mater. Chem. A* **2019**, *7*, 1768.
- [64] D. Song, W. Guo, T. Zhang, P. Lu, A. Guo, F. Hou, X. Yan, J. Liang, *Surf. Innovations* **2019**, *7*, 10.
- [65] C. Kim, P. Srimuk, J. Lee, S. Fleischmann, M. Aslan, V. Presser, *Carbon* **2017**, *122*, 329.
- [66] M. Aslan, M. Zeiger, N. Jäckel, I. Grobelsek, D. Weingarth, V. Presser, *J. Phys.: Condens. Matter* **2016**, *28*, 114003.